Understanding the Electronic Transport of Al−Si and Al−Ge Nanojunctions by Exploiting Temperature-Dependent Bias Spectroscopy

Raphael Behrle, Corban G. E. Murphey, James F. Cahoon, Sven Barth, Martien I. den Hertog, Walter M. Weber,* and Masiar Sistani*

Read Online

ACCESS | Metrics & More | Article Recommendations

ABSTRACT: Understanding the electronic transport of metal−semiconductor heterojunctions is of utmost importance for a wide range of emerging nanoelectronic devices like adaptive transistors, biosensors, and quantum devices. Here, we provide a comparison and in-depth discussion of the investigated Schottky hetero-junction devices based on Si and Ge nanowires contacted with pure single-crystal Al. Key for the fabrication of these devices is the selective solid-state metal−semiconductor exchange of Si and Ge nanowires into Al, delivering void-free, single-crystal Al contacts with flat Schottky junctions, distinct from the bulk counterparts. Thereof, a systematic comparison of the temperature-dependent charge carrier injection and transport in Si and Ge by means of current-bias spectroscopy is visualized by 2D colormaps. Thus, it reveals important insights into the operation mechanisms and regimes that cannot be exploited by conventional single-sweep output and transfer characteristics. Importantly, it was found that the Al−Si system shows symmetric effective Schottky barrier (SB) heights for holes and electrons, whereas the Al−Ge system reveals a highly transparent contact for holes due to Fermi level pinning close to the valence band with charge carrier injection saturation due to a thinned effective SB. Moreover, thermionic field emission limits the overall electron conduction, indicating a distinct SB for electrons.

KEYWORDS: silicon, germanium, aluminum, metal-semiconductor heterostructure, Schottky barrier field-effect transistor
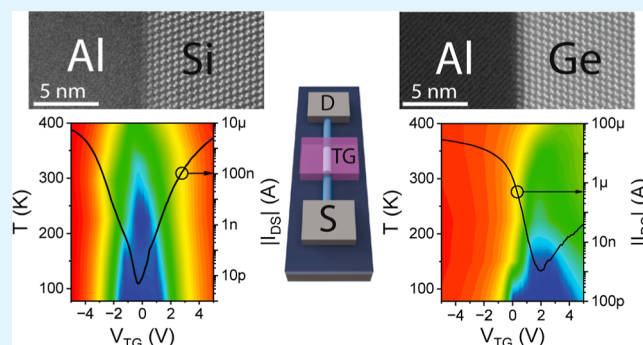
INTRODUCTION

Nanowire (NW)-based Schottky barrier (SB) metal−semi-conductor−metal (MSM) heterostructures are highly interest-ing for emerging applications in nanoelectronics[1,2] and quantum electronics[3,4] that take advantage of their unique physical, electrical, and photonic as well as plasmonic properties.[5,6] Having such a MSM structure allows to electrostatically tune the metal−semiconductor junctions as well as the channel's energy landscape through its implemen-tation in a SB field-effect transistor (SBFET).[2] In this respect, undoped SBFETs show a certain degree of ambipolar charge carrier injection of electrons and holes into the channel, enabling dedicated "More than Moore" paradigms, e.g., reconfigurable FETs (RFETs).[7,8] Importantly, the source/drain contact metal is of high relevance in defining the charge carrier injection capabilities. Here, the Fermi level pinning of the proposed material system is crucial, as it directly affects the SB exhibited to electrons and holes.[9,10] In this respect, works considering Al as source/drain contacts demonstrated promising device concepts, reaching from Si RFETs[11] to negative differential resistance devices based on Ge.[12] From a material point of view, these Al contacts do not form intermetallic phases and provide abrupt and flat metal−semiconductor junctions to both Si and Ge, without the known deficiencies of bulk and layered Al−Si/Ge systems in the nanoscale.[13−15] Importantly, SBFETs show unique character-istics that are fundamentally different from metal−oxide−semiconductor FETs (MOSFETs), allowing for systematic investigations of the injection of charge carriers into the semiconductor, i.e., transport over and/or tunneling through the SB, as well as the transport mechanisms of electrons and holes in the channel.[16,17] In this respect, theoretical investigations on the charge carrier transport in Ni-silicide
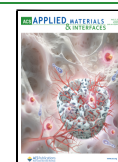
SBFETs were conducted.[18,19] Utilizing the electrostatic tunability of the junctions and channel, the SB shape and its transmissivity can be modulated by varying bias conditions, allowing for the analysis of the transport characteristics of the metal−semiconductor heterostructure in more depth. Investigating the output characteristics over temperature of the NW SBFETs also allows to estimate the activation energy, i.e., the thermal injection capability of charge carriers into the semiconductor.[13,20] Certainly, the theoretical first principles of TCAD modeling of the metal−semiconductor interface would even allow a more detailed analysis of the charge carrier injection contributions, such as thermionic emission (TE), thermally assisted field emission (TFE), and field emission (FE),[21] which in an experimental approach can be merely didactically interpreted.

Importantly, the bias and the gate voltages as well as the temperature highly influence the electronic transport in different manners, which are difficult to analyze by single parameter sweeps. In this sense, the shape of the SB, the tunneling probability, as well as the injection mechanism itself varies and determines the transport. On this matter, bias spectroscopy is a powerful methodology to visualize a detailed image of the electronic transport and indicate different operation regimes due to the fact that multiple transport mechanisms are involved in the operation of SBFETs. Thus, temperature-dependent output and transfer I/V-characteristics are systematically visualized and evaluated. Using 2D colormaps for illustration allows one to obtain a comprehensive picture of the influence of the different parameters on the transport mechanisms. A key technological breakthrough that is allowing such measurements on Ge bottom-up NWs is a novel growth mechanism incorporating an intrinsic phenyl ligand surface passivation during synthesis (cf. Methods section).[22] Till now such an in-depth electronic transport investigation of Al-group IV metal−semiconductor heterostructures is missing. Having physically and electrically equal Al leads to both Si and Ge provides a unique opportunity for insights and comparisons that might be useful for future applications of group IV SBFETs with monolithic Al contacts.

■ RESULTS AND DISCUSSION

In this study, nominally intrinsic, bottom-up grown, Si and Ge NWs are contacted by single-crystalline Al leads, where a rapid thermal annealing (RTA) process initiates a metal−semiconductor exchange reaction that forms the desired MSM heterostructures (cf. Methods section).[13,23] Note that prior to integration, the ⟨112⟩ Si NWs are passivated with a 9 nm thick thermally grown SiO_2. Due to the absence of a stable native oxide, the ⟨111⟩ Ge NWs were conformly covered in a 10 nm thick atomic layer-deposited Al_2O_3 shell. Importantly, these passivation layers also act as gate oxide. Notably, Ge NWs as well as any Ge surface are prone to exhibit strong transient effects due to the presence of Ge_xO_y at the semiconductor-high-κ (here: Al_2O_3) interface.[24,25] In this respect, Hanrath and Korgel have identified "slow" interface trap states to be associated to an enhancement of the p-type behavior of Ge, whereas "fast" interface states are responsible for recombination processes.[26] After drain/source contact formation (here: Al), a top-gate (TG), consisting of Ti/Au, covering the interfaces and the semiconducting channel is fabricated to realize a SBFET.[1,27] Both the Al-Si-Al and Al-Ge-Al MSM structures exhibited a nominal d_{NW} of ≈70 nm and a L_{NW} of ≈1 μm (cf. Methods section). The 3D illustration in Figure 1a
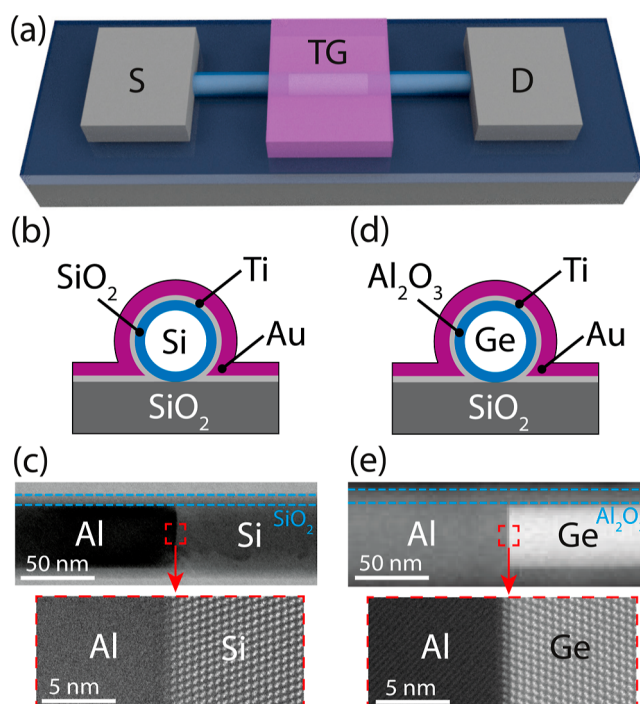

Figure 1. (a) 3D illustration schematically showing the SBFET architecture. The gate-stack for the Al−Si and Al−Ge devices is depicted in (b,d), respectively. Contrast-enhanced HAADF STEM images showing the junction abruptness of the Al−Si (c) and Al−Ge (e) junctions.

shows the fabricated devices. Additionally, the discussed gate-stack of the Al-Si-Al device is shown in Figure 1b and that of the Al-Ge-Al device in Figure 1d. Importantly, the same materials—except for the semiconductor NW and gate oxide—were used, allowing an appropriate comparison of the Al-group IV heterostructures. Applying a bias voltage to the drain/source contacts as well as the TG allows for the operation of the device in different regimes, enabling detailed investigations of the transport mechanism of the proposed material systems.

Bright field (BF) and high-angle annular dark-field (HAADF) scanning transmission electron microscopy (STEM) images of the Al−Si NW interface (cf. Figure 1c) reveal the abrupt and monolithic nature of the junction formed after the thermally induced exchange reaction, performed at a temperature of T = 773.15 K. In equal measure, but at a temperature of 673.15 K, the Al−Ge exchange mechanism is initiated (cf. Figure 1e). Note that detailed investigations on the Al−Si as well as on the Al−Ge exchange mechanism were carried out in the past.[13,23]

Figure 2a shows the obtained transfer characteristics of the proposed Al−Si/Ge−Al SBFETs, sweeping the voltage V_{TG} from 5 to −5 V and applying drain/source biases V_{DS} ranging from 0.25 to 2 V. Note that $V_D = -V_S$ and $V_{DS} = V_D - V_S$. Analyzing the general appearance of the two sets of curves (Al−Si vs Al−Ge) reveals one of the main differences between the two material systems integrated in the proposed SBFET architecture. In the Al-Si-Al system, a relatively equal electron (I_D at V_{TG} = 5 V) and hole (I_D at V_{TG} = − 5 V) current is evident, whereas the hole transport ($V_{TG} < 0$ V) in the Al-Ge-Al system is dominant in comparison to the electron current. This can be attributed to the difference in the Fermi level pinning of the two systems, where the Fermi level at the Al−Si
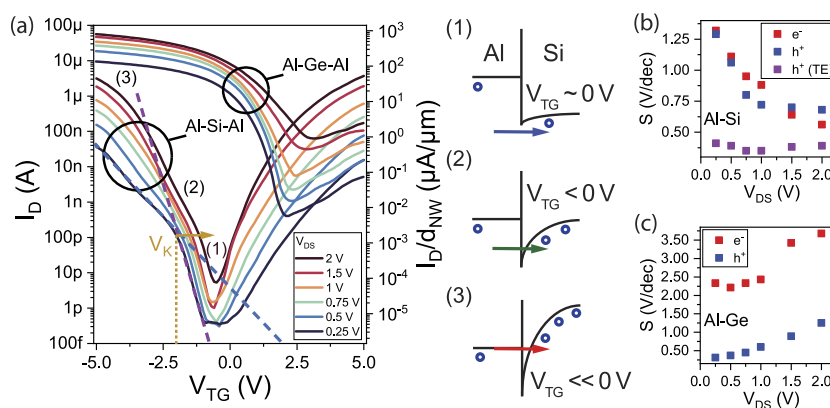
Figure 2. (a) Transfer characteristics at different V_{DS} at $T = 295$ K of the Al−Si and Al−Ge SBFETs. Notably, for $V_{DS} = 0.25$ V at $V_{TG} = -1.95$ V of the Al−Si SBFET, a kink is evident, indicating the transition from TE to TFE/FE. Left to (a), (1−3) illustrate the different injection mechanisms (here: holes) in terms of simplified band diagrams. (b) Extracted steepest inverse subthreshold slopes S $[\Delta V_{TG}/\Delta \log(I_D)]$ of the Al−Si SBFET. The violet symbols show the slopes in the TE regime. (c) Slopes S of the Al−Ge SBFET increasing with higher applied bias V_{DS} due to the reduced bandgap of Ge.

interface pins near the middle of the Si bandgap, leading to a dedicated electron and hole SB.[9] In contrast, the Al−Ge interface has the Fermi level pinning close to the valence band, leading to dominant hole injection and thus to a highly transparent quasi-ohmic contact.[28,29] In the transfer characteristic (cf. Figure 2a), the high transparency of the Al−Ge junction[30] gets evident due to the relatively high and temperature-stable on-current at $V_{TG} < 0$ V. For further clarification, the output characteristic at $V_{TG} < 0$ V is investigated, revealing a highly linear behavior at low V_{DS} (cf. inset in Figure 5b). Additionally, the significantly lower bandgap of Ge $[E_g(\text{Ge}) = 0.67$ eV$]$ in comparison to Si $[E_g(\text{Si}) = 1.12$ eV$]$ becomes apparent due to the fact that the on- and off-currents also strongly depend on the SB height, which needs to be overcome by charge carriers. Therefore, the p-type currents of the Al−Ge material system are higher than those for the Al−Si material system.[31] In this regard, electron and hole mobility would need to be considered, as high mobilities lead to higher drain currents and switching speeds. However, as extracting exact mobility values is difficult for bottom-up grown NWs[32] due to their low gate oxide capacitance hindering C/V measurements,[33] no values can be given for the NWs in this work. Another important aspect becomes evident by observing the steepness of the slopes [cf. Figure 2b (Si) and Figure 2c (Ge)]. Notably, in the p-branch of the Al-Si-Al device, a characteristic kink at the "kink" voltage V_K is observable, see Figure 2a, indicating the transition from TE (charge carrier injection over the barrier) to TFE/FE (charge carrier injection via tunneling) dominated currents,[16] where the violet dashed line indicates the TE slope and the blue dashed line indicates the TFE/FE slope. As shown in Figure 2a, the different regimes can be associated with specific band bending grades and, thereof, injection mechanisms. Illustration (1) shows the case at $V_{TG} \approx 0$ V, where TE is the dominant transport mechanism, as charge carriers can only overcome the SB for channel injection because band bending and therefore sufficient SB thinning are not present. Thus, tunneling does not contribute to charge carrier injection. As shown in (2), further bending the bands by operating the device in stronger accumulation ($V_{TG} \ll 0$ V) TFE/FE gets more dominant due to the fact that the SB is getting thinner, allowing a stronger tunneling contribution, which gets evident by a shallower slope.[31] Interestingly, V_K shifts from −1.95 V at

$V_{DS} = 0.25$ V to $V_K = -1.16$ V at $V_{DS} = 2$ V as the bands bend progressively downward by increasing V_{DS}, and thus TFE/FE dominates the charge carrier injection at lower V_{TG} again due to stronger band bending. This scenario is illustrated in (3). In this context, it needs to be considered, that an increased number of charge carriers in the channel [cf. hole injection in (1−3), Figure 2a] further enhances the band bending, favoring the injection of charge carriers.[27] Importantly, the transition from TE to TFE/FE was already described by simulations.[31,34] In terms of theoretical investigations of the band bending mechanism, the charge carrier injection related to SBFETs as well as the electrostatic gating capabilities were also analyzed in depth by physics-based simulations by Roemer et al.[18,19] Due to the use of transiently stable Si NWs and an expected low interface trap state density between Si and SiO$_2$ as gate oxide, it is possible to show the transition from TE to TFE/FE with respect to a slope change here also experimentally. Figure 2b illustrates the steepest extracted inverse subthreshold slopes, S $= \Delta V_{TG}/\Delta \log(I_D)$ in the subthreshold regime of the Al−Si SBFET for electron and hole conduction. Importantly, in the TE transport, the SB height dominates the injection. Thus, the inverse subthreshold slope remains constant (violet symbols) in the range of ≈0.4 V/dec and shows that the device geometry does not suffer from short channel effects, such as drain-induced barrier lowering. In contrast, when TFE/FE is getting dominant, the slope becomes more shallow in comparison to TE due to tunneling transport.[20] However, with higher applied drain/source bias (blue symbols: p-type and red symbols: n-type), the inverse subthreshold slope approaches values ranging from ≈1.3 V/dec at $V_{DS} = 0.25$ V to ≈0.6 V/dec at $V_{DS} = 2$ V. Due to stronger band bending induced by higher applied biases, the tunneling barrier becomes thinner and thus enables more efficient injection of charge carriers; see (3). Remarkably, this kink is merely visible in the p-branch of the transfer characteristic and is not observable in the n-branch ($V_{TG} > 0$ V). We speculate that a slightly higher SB height evident for electrons leads to diminishing of the kink in the n-branch. In contrast, the Al−Ge SBFET does not exhibit a kink in the slope due to the quasi-ohmic contact for the injection of holes (cf. Figure 2c). Nevertheless, the kink could also be present, but could fall into the increased source/drain leakage and thus not be visible in the I/V data. Remarkably, here the slope increases, applying higher V_{DS} as the smaller bandgap
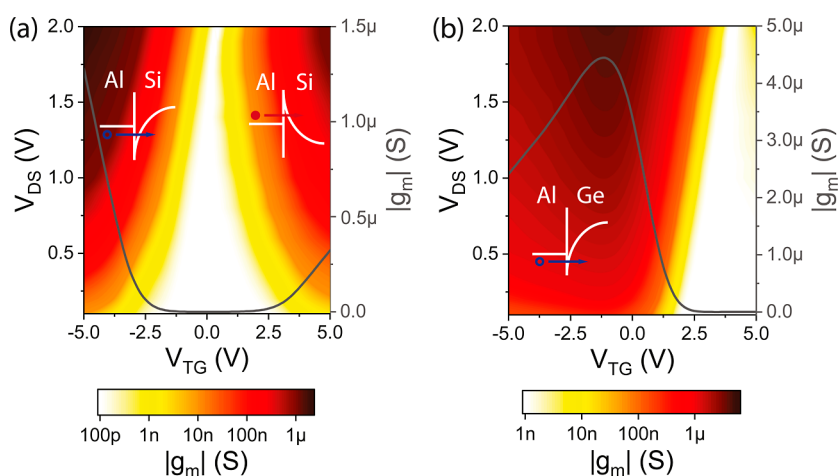
Figure 3. Transconductance $|g_m|$ maps with V_{DS} ranging from 0.1 to 2 V derived from the transfer characteristics of an (a) Al−Si SBFET and an (b) Al−Ge SBFET. Additionally, g_m vs V_{TG} at $V_{DS} = 1$ V is plotted as a solid line and indicated on the right gray y-axis in both plots. The insets depict schematic band diagrams of both systems.
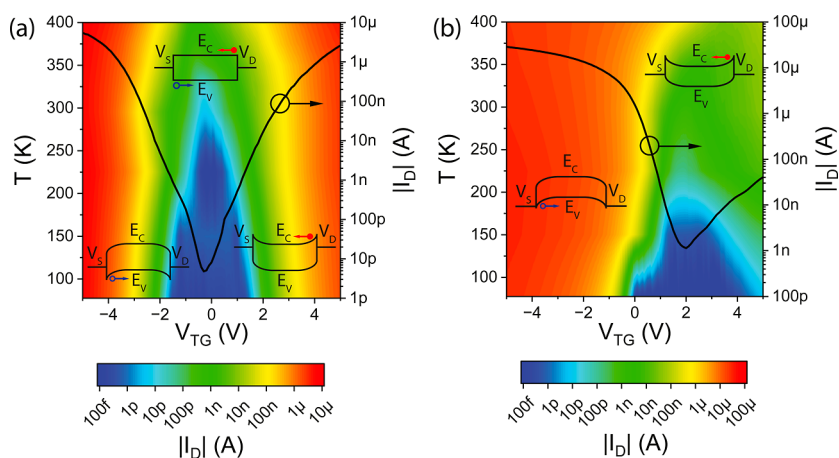

Figure 4. Temperature-dependent transfer characteristic maps of an (a) Al−Si and an (b) Al−Ge SBFET at $V_{DS} = 1$ V. The black curve belonging to the right y-axis shows the transfer characteristic at $T = 295$ K. The insets illustrate the schematic band diagrams of the corresponding predominant transport regimes.

leads to a significant increase in the off-current caused by an increased number of charge carriers in the channel, screening the transition from TE to TFE/FE. In contrast to the relatively symmetric slopes of the n- and p-branch of the Al−Si SBFET devices, the slopes for the Al−Ge SBFET differ, which is an indication of different injection capabilities of electrons and holes, mainly caused by the differences of the Fermi level pinning of the systems. Considering the Al−Si material system, a close-to-midgap pinning is evident, causing similar SBs for electrons and holes, whereas for Al−Ge junctions, the Fermi level pins are close to the valence band of Ge.[9] Therefore, in the Al−Ge material system, a dominant p-type behavior is observed, also causing differences in the inverse subthreshold slope characteristics in comparison to the Al−Si material system.[31]

Furthermore, analyzing the transfer characteristics (cf. Figure 2a) allows us to extract the transconductance $g_m = dI_D/dV_{TG}$. Consequently, we give a qualitative measure of the input to output response in terms of the inverse subthreshold slope and thus an in-depth insight on the transport phenomena of the proposed material systems. Figure 3 shows the transconductance g_m extracted with V_{DS} ranging from 0.1 to 2 V and V_{TG} ranging from −5 to 5 V for the Al−Si (Figure 3a)

and the Al−Ge (Figure 3b) SBFETs. Interestingly, analyzing the Al−Si SBFET, an asymmetric $|g_m|$ value at $|V_{TG}| = 5$ V is obvious which correlates with the transfer characteristic shown in Figure 2a. At $V_{TG} \gg 0$ V, $|g_m|$ values of 313 nS (4.35 μS/μm) and 1.27 μS (17.64 μS/μm) are achieved in the n- and p-type branch, respectively, at $V_{DS} = 1$ V. Another important feature of the Al−Si SBFET is the steady slope of g_m, even at $|V_{TG}| = 5$ V, required for electronic devices, e.g., amplifiers.[35] Here, we assume g_m saturation for higher $|V_{TG}|$. In contrast to the Al−Si SBFET, the transconductance g_m of the Al−Ge SBFET shown in Figure 3b shows no steadily increasing slopes in strong accumulation, instead exhibiting a degradation of g_m in the p-branch. Interestingly, such a degradation is typically visible in SBFETs with distinct barriers at specific bias conditions.[17] In this context, it needs to be distinguished between junction and channel resistance contributions, whereas g_m degradation is commonly attributed to surface roughness scattering as well as to the total resistance (junction resistance and channel resistance). In the Al−Ge SBFET, the Fermi level pins are close to the valence band (see inset in Figure 3b) and thus enable efficient injection of holes into the semiconductor. In this case, the saturation and consequently the degradation becomes evident at any bias condition
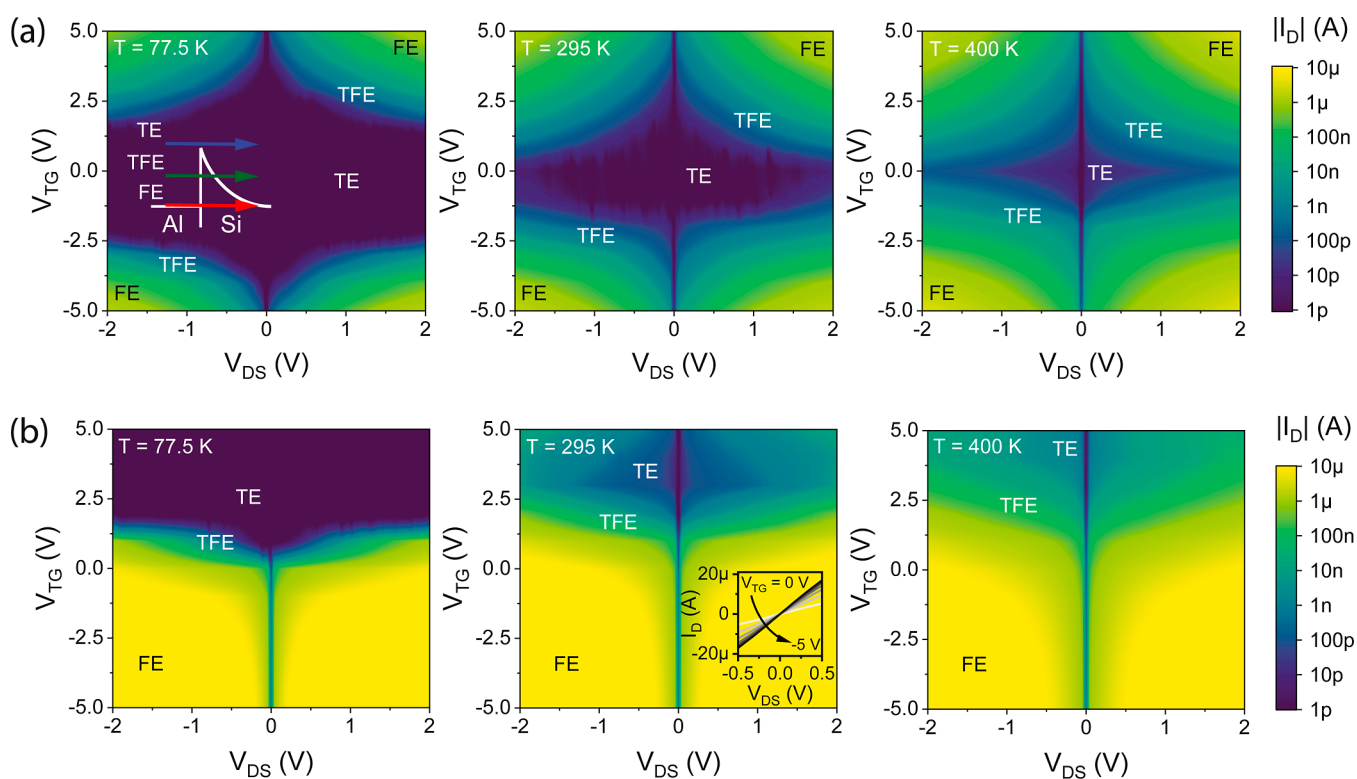
Figure 5. Output characteristic maps in dependence of the applied TG voltage V_{TG} at T = 77.5, 295, and 400 K for an (a) Al−Si SBFET and an (b) Al−Ge SBFET, respectively. TE, TFE, and FE regimes are didactically stated at the corresponding regimes. The inset in (a) illustrates the injection mechanism for electrons. The inset in (b) at T = 295 K illustrates the linear behavior of the output characteristic at low V_{DS} with V_{TG} ranging from 0 to −5 V, indicating quasi-ohmic Al−Ge junctions.

independently of the applied V_{DS}. Therefore, it can be assumed that the highly transparent (quasi-ohmic) junction with phonon scattering in the Ge channel is the predominant factor in this context.[36] Moreover, higher g_m values are reached in the p-branch (V_{TG} = − 5 V) of the Al−Ge SBFET with 2.44 μS (32.53 $\mu S/\mu m$) in comparison to the Al−Si SBFET (1.27 μS) at V_{DS} = 2 V, which can be attributed to steeper slopes of the p-branch transfer curves (cf. Figure 2c) in the Al−Ge SBFET within the observed regime. Note that the degradation in strong accumulation leads to a maximum g_m = 4.43 μS (59.07 $\mu S/\mu m$) at V_{TG} = − 1.19 V. Remarkably, the g_m maximum even occurs at low $|V_{TG}|$ values, caused by a shift of the transfer characteristic (cf. Figure 2a) evident in the Al−Ge system, which can be elaborated by "slow" surface trap states induced shifting toward more dominant p-type behavior.[24] Due to weak electron conduction, in consequence of a relatively high barrier for electrons, g_m merely reaches a value of 2.6 nS (0.03 $\mu S/\mu m$) at V_{TG} = 5 V.

Next, Figure 4 shows the temperature-dependent transfer characteristics of both the Al−Si and Al−Ge SBFETs at V_{DS} = 1 V. Indeed, due to the relatively symmetric Fermi level pinning of Al to Si, a symmetric transport, with V_{TG} = 0 V being the vertical symmetry axis, is visible, which is confirming our initial assumption. Note that the insets shown in Figure 4a illustrate the schematic band diagrams in the corresponding V_{TG} regimes without an applied source/drain bias. Importantly, at V_{TG} = 0 V, dedicated barriers for electrons as well as holes are evident, leading to low off-currents in the 100 fA-regime (minimum resolution of the measurement equipment). Elevating the temperature leads to an increased off-current due to thermally excited charge carriers. However, considering the

current in the n- and p-branch, transiently stable operation modes are observed over the investigated temperature regime from 77.5 to 400 K, proving sufficient operation of the Al−Si material system in the investigated regime. The Al−Ge system, shown in Figure 4b, reveals strong temperature dependencies, which can be attributed to the reduced bandgap of Ge in comparison to Si as well as strong Fermi level pinning close to the valence band, leading to a high contribution of thermally excited charge carriers easily overcoming the low SB exhibited to holes. Moreover, the facts of a smaller bandgap as well as lower SB are becoming apparent, observing the off-current, which shows a stronger temperature dependency in comparison to the Al−Si material system and distributes over a wider V_{TG}. Considering the current in the p-branch, remarkably high values in the 10 μA-regime are evident, further revealing dominant p-type characteristic of the Al−Ge SBFET.

For more detailed investigations on the bias-dependent transport, the output characteristics at different temperatures of the Al−Si (Figure 5a) and Al−Ge (Figure 5b) SBFETs are analyzed. The inset in Figure 5a (Al−Si at T = 77.5 K) illustrates the three main contributions relevant to charge carrier injection. Here, TE is the contribution originating from charge carriers injected over the SB barrier into the semiconductor; see also band diagram (1) in Figure 2a. Importantly, this contribution increases with elevated temperatures due to thermally excited charge carriers overcoming the barrier. Next, FE is considered, which is the contribution originating from the Fermi level pinning of the metal into the semiconductor through tunneling. Here, the charge carriers exhibit minimal potential energy but are efficiently injected in the case of high biases (here: $|V_{DS}|$ = 2 V and $|V_{TG}|$ = 5 V)
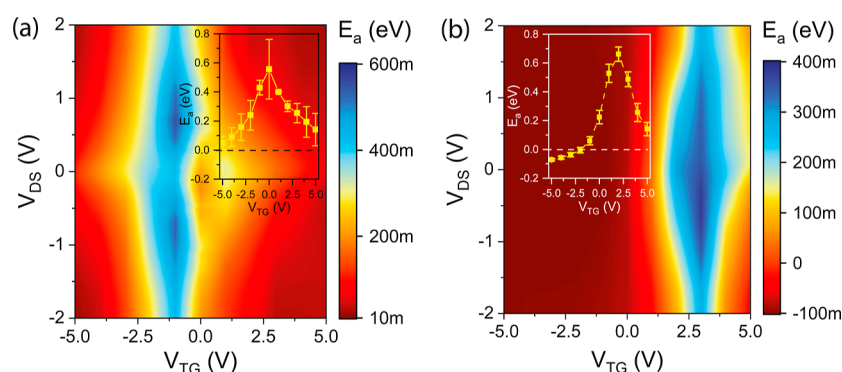
Figure 6. Activation energy maps extracted from output I/V data over temperature of the (a) Al−Si and the (b) Al−Ge SBFET. The insets show the intrinsic activation energy in dependence of V_{TG}. The error bars represent the standard deviation of three similar SBFETs for both material systems.

consequently leading to strong band bending and thus thinner tunneling barriers enabling efficient injection of charge carriers, see also band diagram (3) in Figure 2a. In this context, the transmissivity T_{FE} in the case of FE—and considering WKB approximation—is given as $T_{FE} \approx \exp\left(-\frac{4\sqrt{2m^*}\Phi^{3/2}}{3q\hbar\varepsilon}\right)$, where m^* is the tunneling effective mass, Φ is the SB height, and ε is the electric field, which directly influences the barrier width. Finally, TFE is a mixed transport mechanism of TE and FE, where thermally excited charge carriers can tunnel through the remaining SB; see also band diagrams (2) and (3) in Figure 2a. Again, applying higher biases, i.e., thinning the tunneling barrier, allows an efficient injection via this transport mechanism. The output characteristics of the Al−Si SBFET (cf. Figure 5a) reveal a vertical (V_{DS} = 0 V) and a horizontal (V_{TG} = 0 V) symmetry axis, further proving the symmetrical nature of the Al−Si system. At T = 77.5 K, charge carrier transport is merely possible via TFE and FE due to frozen-out charge carriers not being able to overcome the barrier caused by the lack of thermal excitation. However, elevating the temperature, thus thermally exciting charge carriers, leads to carrier injection even at lower bias voltages. In comparison, the Al−Ge SBFET exhibits only one vertical symmetry axis at V_{DS} = 0 V due to its asymmetric Fermi level pinning, with the Fermi level being close to the valence band. Considering T = 77.5 K, only a negligible increase in the current with increasing |V_{DS}| is observable, which is related to minimal thermal excitation and the dominance of the quasi-ohmic contact between Al and Ge, which is defined by dominant thermal-independent tunneling.[14] Given the combination of a low SB height and efficient band bending yielding an ultrathin barrier, most holes seem to tunnel into the valence band with a high transmission probability. Evidence of this is given in Figure 6b, where near-zero and slightly negative effective SB heights were extracted.[30] We interpret this as a strong indicator for quasi-ohmic contacts, as charge carriers (here: holes) do not experience a thermal energy barrier to overcome the metal−semiconductor junction. Furthermore, an increase in V_{TG} and/or V_{DS} does not lead to sufficient band bending, enabling TFE/FE in this regime. Analyzing the transport at elevated temperatures shows that the FE remains temperature-independent, but the TE in the n-branch ($V_{TG} \gg 0$ V) increases due to thermally excited charge carriers.

Finally, upon processing the output I/V data shown in Figure 5, the activation energy E_a of the material systems can be evaluated (see Figure 6). The basis for the calculation is the TE current model adapted to be suitable for the experimental approach used here. Hence, the voltage between the metal and semiconductor cannot be considered due to the experimental setup, and a simplified model needs to be applied, which is valid for an applied bias voltage exceeding $3k_BT/q$ (76 mV at T = 300 K).[37] Consequently, $J_{TE}(T) = A^*T^2\exp\left(\frac{-qE_a}{k_BT}\right)$, where J_{TE} is the measured current density, A^* is the effective Richardson constant, T is the corresponding temperature, and E_a is the total effective activation energy.[37] Note that this model does not allow a distinction between the proposed transport mechanisms, as in the experimental setup, the total current is measured and thus merely gives an estimation of E_a. Rearranging the equation accordingly, a Richardson plot is obtained allowing the extraction of the activation energy, i.e., the energy required to inject charge carriers into the semiconductor. Using this approach, the V_{TG}-dependent intrinsic activation energy is obtained (cf. insets in Figure 6) by fitting E_a to V_{DS} = 0 V. Moreover, performing a separate measurement with a wider V_{DS} range and without fitting to V_{DS} = 0 V, a 2D colormap in dependence of V_{TG} and V_{DS} can be created, as shown in Figure 6. As shown in the map and in the inset, the activation energy E_a of the Al−Si SBFET (cf. Figure 6a) exhibits positive and similar E_a values at any measured operation point, indicating dedicated SBs for electrons and holes, further demonstrating the relative midgap pinning of Al to the Si bandgap. Remarkably, considering the intrinsic E_a (cf. inset of Figure 6a), a vertical symmetry axis at V_{TG} = 0 V is visible. Notably, in the off-state of the Al−Si SBFET, a relatively high activation energy is evaluated, corresponding well with previously shown results (cf. Figure 2a). In comparison, the Al−Ge SBFET shown in Figure 6b exhibits negative E_a values for hole conduction, further supporting the presence of quasi-ohmic contacts in the p-branch, caused by strong Fermi level pinning close to the valence band.[28,38] This was also shown in carbon nanotubes with Pd contacts also claiming quasi-ohmic injection of charge carriers.[39] Observing electron conduction at positive V_{TG} reveals that a dedicated barrier becomes evident. Moreover, a shift of the off-state into the n-branch takes place, further enhancing the p-branch and thus favoring hole conduction, which is caused by "slow" interface traps.[24] Additionally, the use of Al_2O_3 as gate oxide (cf. Figure 1d,e) is further pushing the Al−Ge SBFET to dominant p-mode operation.[40]

CONCLUSIONS

In conclusion, we have analyzed Al−Si and Al−Ge-based SBFETs in terms of temperature-dependent bias spectroscopy and provided an in-depth analysis of the involved electronic transport mechanisms. Remarkably, using single-crystalline Al as drain/source contacts allows for a comparison of the transport properties of Si and Ge SBFETs. Output and transfer characteristic measurements and systematic evaluations allow us to investigate the effects of Fermi level pinning, which in the Al−Ge SBFET leads to dominant p-type conduction and quasi-ohmic contacts for hole conduction, while Si-based SBFETs show equal charge carrier injection capabilities of electrons and holes. In comparison to single parameter sweeps, evaluating g_m-, I_D-, and E_a-maps allows us to gain important insights into the dependence of various parameters directly influencing the transport behavior. Most notably, the presented investigations of the bias and temperature-dependent transport in Al−Si and Al−Ge nanojunctions contribute to a better understanding of the operation regimes and transport mechanisms of metal-group IV-based SBFETs, which are highly anticipated for the implementation of electronic device functionalities beyond the capabilities of conventional FETs and CMOS devices in general.

METHODS

Si NW Growth. The ⟨112⟩ oriented intrinsic Si NWs were grown in a home-built, hot-wall chemical vapor deposition (CVD) system described previously using silane and HCl gases, hydrogen carrier gas, and Au nanoparticle catalysts of diameter 80 nm. NW growth was performed at 753 K with 2 standard cubic centimeters per minute (sccm) of SiH_4, 4 sccm of HCl, and 194 sccm of H_2 at 20 Torr total reactor pressure for 20 min until the desired NW length of 20 μm was obtained. The Si NWs have diameters d_{NW} of ≈70 nm. Subsequent to the growth, the Si NWs were thermally oxidized at $T = 1174$ K in O_2 atmosphere for 3 min and annealed for another 3 min in N_2 atmosphere to form a high-quality 9 nm thick SiO_2 gate oxide.

Ge NW Growth. The intrinsic Ge NWs were grown on Ge(111) single-crystal substrates by low-pressure CVD in a cold-wall reactor. Prior to use, the substrates were coated with a 1 nm thick Au film by sputtering. The Ge substrate was heated to 748 K under dynamic vacuum before diphenylgermane (DPG; 40 mg DPG reservoir at 295 K; process pressure $<1 \times 10^{-3}$ mbar) was introduced to the CVD chamber for 20 to 30 min, keeping the precursor at room temperature and applying dynamic vacuum. The Au seeds act as catalytic sites for the precursor decomposition. Similar growth procedures using the same precursor under LPCVD conditions have been reported in the literature.[22,41] After the growth of the ≈70 nm thick Ge NWs, they were conformally coated with 10 nm of Al_2O_3 by atomic layer deposition at a temperature of $T = 474$ K.

SBFET Fabrication. The passivated Si/Ge NWs were drop-casted onto a 100 nm thick thermally grown SiO_2 layer atop a 500 μm thick highly p-doped Si substrate. Al contacts to the Si/Ge NWs were fabricated by a combination of electron beam lithography, 15 s of BHF (7:1) etching to remove the SiO_2/Al_2O_3 shell at the contact area, 125 nm Al sputter deposition, and lift-off techniques. A successive thermally induced exchange reaction by RTA at a temperature of $T = 774$ K/$T = 674$ K in forming-gas atmosphere initiates the substitution of Si/Ge by Al. After annealing, the semiconductor channel length was ≈1 μm in length with a NW diameter of ≈70 nm for the Si NWs as well as Ge NWs (without passivation). Facilitating this heterostructure formation scheme allows the integration of single-crystalline monolithic Al−Si/Al−Ge NW heterostructures. The Ω-shaped Ti/Au TG covering the interfaces as well as semiconductor channel was fabricated using a combination of electron beam lithography, Ti/Au evaporation (10 nm Ti, 100 nm Au), and lift-off techniques.

BF and HAADF STEM. BF and HAADF STEM (zoom) was performed on Al-Si-Al and Al-Ge-Al NW heterostructures fabricated on 40 nm thick Si_3N_4 membranes using a probe-corrected FEI Titan Themis, working at 200 kV. The Al−Si interface in the shown images is viewed along the [110] direction of observation of the Si crystal. {111} planes are visible in the Al region. HAADF images of the Al−Ge interface are shown, where the Ge crystal is in the [110] direction of observation. Similarly, {111} planes are visible in the Al region.

Electrical Measurements. The electrical measurements were performed by using a combination of a semiconductor analyzer (HP 4156B) and a probe station. To minimize the influence of ambient light, as well as electromagnetic fields, the probe station is placed in a dark box. For applying the bias voltage, the following holds: $V_{DS} = V_D - V_S$ and $V_D = -V_S$. Temperature-dependent measurements as well as measurements to extract the activation energy were performed in a vacuum using a cryogenic probe station (Lake Shore PS-100) and a semiconductor analyzer (Keysight B1500A).

AUTHOR INFORMATION

Corresponding Authors

Masiar Sistani − *Institute of Solid State Electronics, Technische Universität Wien, Vienna 1040, Austria;* orcid.org/0000-0001-5730-234X; Email: walter.weber@tuwien.ac.at

Walter M. Weber − *Institute of Solid State Electronics, Technische Universität Wien, Vienna 1040, Austria;* orcid.org/0000-0001-9504-5671; Email: masiar.sistani@tuwien.ac.at

Authors

Raphael Behrle − *Institute of Solid State Electronics, Technische Universität Wien, Vienna 1040, Austria;* orcid.org/0000-0003-4446-1450

Corban G. E. Murphey − *Department of Chemistry, University of North Carolina at Chapel Hill, Chapel Hill, North Carolina 27599, United States*

James F. Cahoon − *Department of Chemistry, University of North Carolina at Chapel Hill, Chapel Hill, North Carolina 27599, United States*

Sven Barth − *Physics Institute and Institute of Inorganic and Analytical Chemistry, Goethe Universität Frankfurt, Frankfurt am Main 60438, Germany;* orcid.org/0000-0003-3900-2487

Martien I. den Hertog − *Institut Néel, CNRS UPR2940, Grenoble 38042, France;* orcid.org/0000-0003-0781-9249

Complete contact information is available at:
https://pubs.acs.org/10.1021/acsami.3c18674

Notes

The authors declare no competing financial interest.

■ REFERENCES

(1) Sharma, B. *Metal-Semiconductor Schottky Barrier Junctions and Their Applications*; Springer Science & Business Media, 2013; p 386.

(2) Schwarz, M.; Vethaak, T. D.; Derycke, V.; Francheteau, A.; Iniguez, B.; Kataria, S.; Kloes, A.; Lefloch, F.; Lemme, M.; Snyder, J. P.; Weber, W. M.; Calvet, L. E. The Schottky barrier transistor in emerging electronic devices. *Nanotechnology* 2023, 34, 352002.

(3) Ridderbos, J.; Brauns, M.; De Vries, F. K.; Shen, J.; Li, A.; Kölling, S.; Verheijen, M. A.; Brinkman, A.; Van Der Wiel, W. G.; Bakkers, E. P.; Zwanenburg, F. A. Hard superconducting gap and diffusion-induced superconductors in Ge-Si nanowires. *Nano Lett.* 2020, 20, 122−130.

(4) Delaforce, J.; Sistani, M.; Kramer, R. B.; Luong, M. A.; Roch, N.; Weber, W. M.; den Hertog, M. I.; Robin, E.; Naud, C.; Lugstein, A.; Buisson, O. Al−Ge−Al Nanowire Heterostructure: From Single-Hole Quantum Dot to Josephson Effect. *Adv. Mater.* 2021, 33, 2101989.

(5) Falk, A. L.; Koppens, F. H. L.; Yu, C. L.; Kang, K.; de Leon Snapp, N.; Akimov, A. V.; Jo, M.-H.; Lukin, M. D.; Park, H. Near-field electrical detection of optical plasmons and single-plasmon sources. *Nat. Phys.* 2009, 5, 475−479.

(6) Sistani, M.; Bartmann, M. G.; Güsken, N. A.; Oulton, R. F.; Keshmiri, H.; Luong, M. A.; Momtaz, Z. S.; Den Hertog, M. I.; Lugstein, A. Plasmon-Driven Hot Electron Transfer at Atomically Sharp Metal-Semiconductor Nanojunctions. *ACS Photonics* 2020, 7, 1642−1648.

(7) Sacchetto, D.; Leblebici, Y.; De Micheli, G. Ambipolar gate-controllable SiNW FETs for configurable logic circuits with improved expressive capability. *IEEE Electron Device Lett.* 2012, 33, 143−145.

(8) Böckle, R.; Sistani, M.; Lipovec, B.; Pohl, D.; Rellinghaus, B.; Lugstein, A.; Weber, W. M. A Top-Down Platform Enabling Ge Based Reconfigurable Transistors. *Adv. Mater. Technol.* 2022, 7, 2100647.

(9) Clark, R. Emerging Applications for High-k Materials in VLSI Technology. *Materials* 2014, 7, 2913−2944.

(10) Tung, R. T. Recent advances in Schottky barrier concepts. *Mater. Sci. Eng., R* 2001, 35, 1−138.

(11) Böckle, R.; Sistani, M.; Bažíková, M.; Wind, L.; Sadre-Momtaz, Z.; den Hertog, M. I.; Murphey, C. G.; Cahoon, J. F.; Weber, W. M. Reconfigurable Complementary and Combinational Logic Based on Monolithic and Single-Crystalline Al-Si Heterostructures. *Adv. Electron. Mater.* 2023, 9, 2200567.

(12) Behrle, R.; Den Hertog, M. I.; Lugstein, A.; Weber, W. M.; Sistani, M. Bias Spectroscopy of Negative Differential Resistance in Ge Nanowire Cascode Circuits. In *European Solid-State Device Research Conference*: Lisbon, 2023; pp 37−40.

(13) Wind, L.; Böckle, R.; Sistani, M.; Schweizer, P.; Maeder, X.; Michler, J.; Murphey, C. G.; Cahoon, J.; Weber, W. M. Monolithic and Single-Crystalline Aluminum-Silicon Heterostructures. *ACS Appl. Mater. Interfaces* 2022, 14, 26238−26244.

(14) Behrle, R.; Bažíková, M.; Barth, S.; Weber, W. M.; Sistani, M. Mapping Electronic Transport in Ge Nanowire SBFETs: From Tunneling to NDR. In *2023 IEEE Nanotechnology Materials and Devices Conference (NMDC)*, 2023; pp 889−894.

(15) Yue, J.; Funsten, W.; Taylor, R. Stress Induced Voids in Aluminum Interconnects During IC Processing. In *23rd International Reliability Physics Symposium*, 1985; pp 126−137.

(16) Jeon, D. Y.; Pregl, S.; Park, S. J.; Baraban, L.; Cuniberti, G.; Mikolajick, T.; Weber, W. M. Scaling and Graphical Transport-Map Analysis of Ambipolar Schottky-Barrier Thin-Film Transistors Based on a Parallel Array of Si Nanowires. *Nano Lett.* 2015, 15, 4578−4584.

(17) Park, S. J.; Jeon, D. Y.; Sessi, V.; Trommer, J.; Heinzig, A.; Mikolajick, T.; Kim, G. T.; Weber, W. M. Channel Length-Dependent Operation of Ambipolar Schottky-Barrier Transistors on a Single Si Nanowire. *ACS Appl. Mater. Interfaces* 2020, 12, 43927−43932.

(18) Roemer, C.; Darbandy, G.; Schwarz, M.; Trommer, J.; Heinzig, A.; Mikolajick, T.; Weber, W. M.; Iniguez, B.; Kloes, A. Physics-Based DC Compact Modeling of Schottky Barrier and Reconfigurable Field-Effect Transistors. *IEEE J. Electron Devices Soc.* 2022, 10, 416−423.

(19) Roemer, C.; Dersch, N.; Darbandy, G.; Schwarz, M.; Han, Y.; Zhao, Q. T.; Iñíguez, B.; Kloes, A. Compact modeling of Schottky barrier field-effect transistors at deep cryogenic temperatures. *Solid-State Electron.* 2023, 207, 108686.

(20) Jeon, D.-Y.; Zhang, J.; Trommer, J.; Park, S. J.; Gaillardon, P.-E.; De Micheli, G.; Mikolajick, T.; Weber, W. M. Operation regimes and electrical transport of steep slope Schottky Si-FinFETs. *J. Appl. Phys.* 2017, 121, 064504.

(21) Kiziroglou, M.; Li, X.; Zhukov, A.; de Groot, P.; de Groot, C. Thermionic field emission at electrodeposited Ni−Si Schottky barriers. *Solid-State Electron.* 2008, 52, 1032−1038.

(22) Barth, S.; Jimenez-Diaz, R.; Samà, J.; Daniel Prades, J.; Gracia, I.; Santander, J.; Cane, C.; Romano-Rodriguez, A. R. Localized growth and in situ integration of nanowires for device applications. *Chem. Commun.* 2012, 48, 4734−4736.

(23) El hajraoui, K.; Luong, M. A.; Robin, E.; Brunbauer, F.; Zeiner, C.; Lugstein, A.; Gentile, P.; Rouvière, J. L.; Den Hertog, M. In Situ Transmission Electron Microscopy Analysis of Aluminum−Germanium Nanowire Solid-State Reaction. *Nano Lett.* 2019, 19, 2897−2904.

(24) Hanrath, T.; Korgel, B. A. Chemical Surface Passivation of Ge Nanowires. *J. Am. Chem. Soc.* 2004, 126, 15466−15472.

(25) Sistani, M.; Staudinger, P.; Lugstein, A. Polarity Control in Ge Nanowires by Electronic Surface Doping. *J. Phys. Chem. C* 2020, 124, 19858−19863.

(26) Hanrath, T.; Korgel, B. A. Influence of Surface States on Electron Transport through Intrinsic Ge Nanowires. *J. Phys. Chem. B* 2005, 109, 5518−5524.

(27) Knoch, J.; Zhang, M.; Appenzeller, J.; Mantl, S. Physics of ultrathin-body silicon-on-insulator Schottky-barrier field-effect transistors. *Appl. Phys. A: Mater. Sci. Process.* 2007, 87, 351−357.

(28) Nishimura, T.; Kita, K.; Toriumi, A. Evidence for strong Fermi-level pinning due to metal-induced gap states at metal/germanium interface. *Appl. Phys. Lett.* 2007, 91, 123123.

(29) Sistani, M.; Delaforce, J.; Kramer, R. B.; Roch, N.; Luong, M. A.; Den Hertog, M. I.; Robin, E.; Smoliner, J.; Yao, J.; Lieber, C. M.; Naud, C.; Lugstein, A.; Buisson, O. Highly Transparent Contacts to the 1D Hole Gas in Ultrascaled Ge/Si Core/Shell Nanowires. *ACS Nano* 2019, 13, 14145−14151.

(30) Wind, L.; Sistani, M.; Böckle, R.; Smoliner, J.; Vukušić, L.; Aberl, J.; Brehm, M.; Schweizer, P.; Maeder, X.; Michler, J.; Fournel, F.; Hartmann, J.; Weber, W. M. Composition Dependent Electrical Transport in Si$_{1-x}$Ge$_x$Nanosheets with Monolithic Single-Elementary Al Contacts. *Small* 2022, 18, 2204178.

(31) Beister, J.; Wachowiak, A.; Heinzig, A.; Trommer, J.; Mikolajick, T.; Weber, W. M. Temperature dependent switching behaviour of nickel silicided undoped silicon nanowire devices. *Phys. Status Solidi C* 2014, 11, 1611−1617.

(32) Echresh, A.; Arora, H.; Fuchs, F.; Li, Z.; Hübner, R.; Prucnal, S.; Schuster, J.; Zahn, P.; Helm, M.; Zhou, S.; Erbe, A.; Rebohle, L.; Georgiev, Y. M. Electrical Characterization of Germanium Nanowires Using a Symmetric Hall Bar Configuration: Size and Shape Dependence. *Nanomaterials* 2021, 11, 2917.

(33) Weber, W. M.; Mikolajick, T. Silicon and germanium nanowire electronics: Physics of conventional and unconventional transistors. *Rep. Prog. Phys.* 2017, 80, 066502.

(34) Baldauf, T.; Heinzig, A.; Mikolajick, T.; Weber, W. M. Scaling Aspects of Nanowire Schottky Junction based Reconfigurable Field Effect Transistors. In *Joint International EUROSOI Workshop and*

International Conference on Ultimate Integration on Silicon (EUROSOI-ULIS), 2019; pp 1−4.

(35) Sánchez-Sinencio, E.; Silva-Martínez, J. CMOS transconductance amplifiers, architectures and active filters: A tutorial. *IEE Proceedings: Circuits, Devices and Systems* **2000**, *147*, 3−12.

(36) Purewal, M. S.; Hong, B. H.; Ravi, A.; Chandra, B.; Hone, J.; Kim, P. Scaling of resistance and electron mean free path of single-walled carbon nanotubes. *Phys. Rev. Lett.* **2007**, *98*, 186808.

(37) Rhoderick, E.; Williams, R.. In *Metal-Semiconductor Contacts*; Hammond, P., Grimsdale, R., Eds.; Oxford University Press: Oxford, 1988; p 268.

(38) Tao, M.; Udeshi, D.; Agarwal, S.; Maldonado, E.; Kirk, W. Negative Schottky barrier between titanium and n-type Si for low-resistance ohmic contacts. *Solid-State Electron.* **2004**, *48*, 335−338.

(39) Svensson, J.; Sourab, A. A.; Tarakanov, Y.; Lee, D. S.; Park, S. J.; Baek, S. J.; Park, Y. W.; Campbell, E. E. B. The dependence of the Schottky barrier height on carbon nanotube diameter for Pd−carbon nanotube contacts. *Nanotechnology* **2009**, *20*, 175204.

(40) Berghuis, W. J. H.; Melskens, J.; Macco, B.; Theeuwes, R. J.; Verheijen, M. A.; Kessels, W. M. M. Surface passivation of germanium by atomic layer deposited Al2O3 nanolayers. *J. Mater. Res.* **2021**, *36*, 571−581.

(41) Sistani, M.; Bartmann, M. G.; Güsken, N. A.; Oulton, R. F.; Keshmiri, H.; Seifner, M. S.; Barth, S.; Fukata, N.; Luong, M. A.; Den Hertog, M. I.; Lugstein, A. Nanoscale aluminum plasmonic waveguide with monolithically integrated germanium detector. *Appl. Phys. Lett.* **2019**, *115*, 161107.